Mech. Sci., 17, 783–798, 2026
https://doi.org/10.5194/ms-17-783-2026

Mechanical Sciences
Open Access

Optimal design and validation of a heavy-duty wave compensation parallel platform utilizing the NSGA-III algorithm

Tianzhong Huang[1], **Renjie Luo**[3], **Lifeng Mao**[1], **Jia Wang**[3], **Fei Zhou**[2], **and Guoxing Zhang**[3]

[1]Shanghai Marine Equipment Research Institute, Shanghai 409817, China
[2]Zhejiang College of Security Technology, Wenzhou 325016, China
[3]School of Mechanical Engineering, Jiangsu University of Science and Technology, Zhenjiang 212100, China

Correspondence: Fei Zhou (494839661@qq.com) and Guoxing Zhang (gxzhang@just.edu.cn)

Received: 23 April 2026 – Revised: 3 July 2026 – Accepted: 6 July 2026 – Published: 28 July 2026

Abstract. The optimal design indices of heavy-duty wave compensation parallel mechanisms usually involve trade-off relationships, making multi-objective optimization of great significance for practical engineering applications. This study proposes a multi-objective optimization approach tailored for a heavy-duty wave compensation parallel platform, which integrates an artificial neural network (ANN) surrogate model with an enhanced NSGA-III algorithm. Firstly, a decision-making model is constructed, incorporating the topological parameters and performance indices of the mechanism. Secondly, an explicit surrogate model is developed to establish the relationship between structural parameters and the physical responses of the system using an ANN, thereby enhancing the computational efficiency of the pose-space traversal of the parallel platform. Finally, the NSGA-III algorithm, integrated with reference points and an interference penalty mechanism, is utilized for high-dimensional parameter optimization, while the technique for order preference by similarity to ideal solution (TOPSIS) is employed to achieve collaborative optimization across different objectives. Comparative results indicate that NSGA-III outperforms the traditional NSGA-II algorithm in terms of evaluation metrics. Compared to the initial baseline design, the optimal solution achieves an 18.12 % improvement in dexterity, an 11.78 % reduction in peak driving force, and a 6.85 % enhancement in the condition number, all while reducing actuator stroke. This study provides a valuable reference for the optimal design and prototype development of heavy-duty wave compensation parallel platforms.

1 Introduction

With the continuous advancement of offshore engineering technology and equipment into deep-sea areas, maritime operations such as offshore wind power maintenance, large-scale equipment lifting, and the transfer of personnel and materials have experienced explosive growth (Mu et al., 2026; Niu et al., 2022). As the core passage connecting service operation vessels and offshore fixed platforms, the offshore gangway is a critical piece of equipment for ensuring the safety of personnel and materials. However, the complex and volatile marine environment induces 6-degree-of-freedom motions in the ship, which can easily trigger structural collisions and equipment damage or even threaten the safety of operators. Equipped wave compensation systems at the base of offshore gangways have become a prevailing industry consensus for current deep-sea operations (Liang et al., 2020; Tang et al., 2023).

In recent years, as maritime operations have trended toward large-scale and heavy-load applications, more stringent performance requirements have been imposed on wave compensation equipment. Among various spatial mechanisms, the 6-degree-of-freedom Stewart (1965) parallel mechanism has been widely adopted as the underlying actuator for heavy-duty wave compensation gangways owing to its high structural stiffness, superior load-bearing capacity, and rapid dynamic response (Briot et al., 2015; Yin et al., 2022). In the design of parallel mechanisms, the selection of parameters – such as the radii of the base and platform joints, the joint distribution angles, and the initial height – directly determines the kinematic and dynamic performance across the entire task space (Dasgupta et al., 2000; Gosselin et al., 1991). Highlighting this dependency, Zhang et al. (2022a, b) conducted dynamic modeling and vibration characteristic analysis on parallel antenna structures, demonstrating the critical impact of geometric configurations on overall dynamic stability. Guo et al. (2022a, b) synthesized a URU-RR-URU module antenna by connecting mechanism configuration, and a mechanical analysis of a deployable antenna based on the 3RR-3URU element was carried out. Furthermore, in the broader field of structural optimization, Wang et al. (2025) and Wang et al. (2026) demonstrated that strategically designing geometric configurations based on load paths is highly effective for enhancing the stiffness of Gyroid functionally graded lattice structures. For heavy-duty offshore gangways, any mismatch in geometric dimensions can lead to redundant actuator strokes and low utilization of the ship's deck space. More critically, it can cause certain legs to endure excessive peak driving forces when encountering extreme wave poses (Wang et al., 2017). Furthermore, if the mechanism approaches a singular pose within the workspace, it may experience violent oscillations, leading to mechanical failure (Hsu et al., 2023). Therefore, optimizing the configuration parameters of the parallel platform is a prerequisite for achieving the efficient and stable operation of high-load wave compensation systems.

Current research on wave compensation systems for offshore gangway parallel platforms primarily focuses on the development of low-level control algorithms. In exploring the widespread application of these control technologies across diverse robotic domains, Yu et al. (2026) systematically reviewed the evolution from structural design to intelligent control for soft robots. Similarly, Fallahiarezoodar and Zhu (2025) extensively summarized the control strategies of autonomous space robotic manipulators for on-orbit servicing. Wang et al. (2025) adopted a linear active disturbance rejection control strategy, effectively estimating and compensating for nonlinear loads caused by complex sea states. Li et al. (2024) employed a neural-network-based back propagation proportional integral derivative (BP-PID) algorithm, enhancing the robustness and compensation accuracy of shipborne Stewart platforms. Grewal et al. (2012) utilized linear–quadratic–Gaussian control, significantly improving attitude tracking precision by combining a linear quadratic regulator (LQR) with Kalman filtering. Richter et al. (2017) applied model predictive control to active wave compensation systems, handling the physical saturation constraints of actuators through receding horizon optimization. Chen et al. (2023) proposed a modal space strategy for dynamic decoupling, weakening nonlinear interference between multi-axis hydraulic cylinders. Zhang et al. (2025) proposed a novel method for surface division and conducted verification. However, most of the aforementioned studies are predicated on fixed mechanism dimensions, relying on control algorithms to compensate for physical configuration deficiencies. In the evolution of parallel mechanism topological parameter optimization, early strategies predominantly relied on single-objective optimization. Although algorithms like differential evolution and genetic algorithms have played vital roles (Storn et al., 1997; Holland et al., 1992; Qiang et al., 2019), these conventional swarm intelligence methods are prone to premature convergence when facing the complex nonlinear parameters of the Stewart platform, struggling to escape local optima and effectively handle multimodal functions.

To balance multiple performance indices, Gao et al. (2010) and Abdur et al. (2018) assigned weighting coefficients to different objectives using genetic algorithms to transform multi-objective problems into single-objective evaluations. However, since performance indices are often mutually exclusive, this weight allocation is inherently subjective and difficult to quantify precisely for practical engineering trade-offs (Marler et al., 2010). Additionally, Karaboga and Basturk (2007) and Poli et al. (2007) explored heuristic methods like artificial bee colony and particle swarm optimization to optimize actuator velocity and driving force (Shahbazi et al., 2024). Yet, these methods suffer from low computational efficiency during massive transient force analyses for heavy-duty platforms, yielding incomplete or discontinuous Pareto fronts. To overcome these computational barriers, Jin (2011) and other researchers introduced surrogate-assisted optimization strategies cross-fused with artificial neural networks (ANNs), achieving orders-of-magnitude leaps in optimization efficiency by constructing explicit surrogate models (Bhosekar et al., 2018; Chughet al., 2019; Hornik et al.,1989; Pu et al., 2023; Tao et al., 2025). Furthermore, while the traditional NSGA-II algorithm is widely used, it loses its screening ability in high-dimensional spaces as the number of objectives increases (Deb et al., 2002; Liu et al., 2018; Purshouse et al., 2007). To address this flaw, Deb and Jain (2013) developed the NSGA-III algorithm based on a systematic reference point mechanism, proving its effectiveness in capturing continuous and dense fronts in high-dimensional spaces (Ishibuchi et al., 2016). Simultaneously, Hwang and Yoon (2012) and Shih et al. (2007) established TOPSIS as an effective tool for scientifically selecting the global optimal solution from high-dimensional non-dominated sets. Despite these advances, systematic optimization integrating all of these elements remains scarce. Fundamentally, any advanced control strategy must be built upon a rational physical configuration; otherwise, the system will inevitably be constrained by inherent physical bottlenecks such as actuator output limitations and joint interference. For a 20 t heavy-duty wave compensation platform, achieving a compact, high-capacity, and impact-resistant design urgently requires investigating the multi-objective optimization problem consisting of four core physical indices: maximum actuator stroke, peak driving force, global dexterity, and kinematic isotropy.

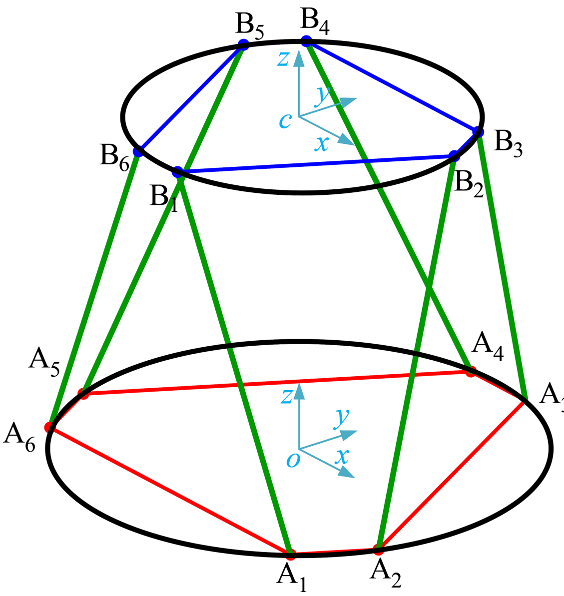

Figure 1. Schematic diagram of the heavy-duty compensation parallel platform mechanism.

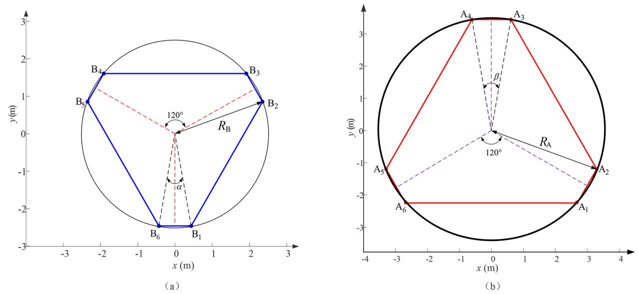

Figure 2. Joint distribution on the moving and base platforms. **(a)** Moving platform. **(b)** Base platform.

Table 1. Structural design variables of the wave compensation platform.

Variable symbol	R_B	R_A	α	β	H
Lower bound (mm)	2000	3000	10	10	4000
Upper bound (mm)	3000	4500	30	30	7000

To address the multi-parameter coupling and complex solving issues in heavy-duty wave compensation parallel platforms, this paper proposes a systematic optimization framework. First, a comprehensive decision model encompassing topological parameters and performance indices is constructed. Second, an ANN is introduced to establish an explicit surrogate model for physical responses. Subsequently, an improved NSGA-III algorithm is employed for high-dimensional optimization to obtain the Pareto optimal front. Finally, the TOPSIS decision-making method is applied to select the global optimal configuration. This study provides a reliable design benchmark for the prototype development of heavy-duty wave compensation equipment.

2 Multi-objective optimization design modeling of heavy-duty compensation parallel platforms

2.1 Establishment of the optimization model

First, two coordinate systems – the moving and fixed frames – are established. The origin O of the fixed coordinate system O-xyz is located at the center of the base platform's joints. The origin C of the moving-coordinate system C-xyz is located at the center of the moving platform's joints. When the moving platform is at its home position, the directions of the x, y, and z axes for both coordinate systems are identical, and the z axis of the fixed coordinate system passes through point C. The orientation of each axis is shown in Fig. 1.

As shown in Fig. 1, points B_1–B_6 are the six joints on the upper platform, used for installation and positioning at the upper-platform connections, and C is the center of the upper joint circle. Points A_1–A_6 are the six joints used for installation and positioning at the lower-platform connections, and O is the center of the lower joint circle. R_B represents the radius of the upper platform's joint circle, and R_A represents the radius of the lower platform's joint circle, while H represents the initial height of the platform. The angle between a pair of adjacent joints on the upper platform is α, and the angle between a pair of adjacent joints on the lower platform is β.

For the heavy-duty compensation parallel platform, five key configuration parameters affecting its kinematic characteristics are selected to form a five-dimensional decision vector $\boldsymbol{x}$:

$$\boldsymbol{x} = [R_B, R_A, \alpha, \beta, H]^T \tag{1}$$

Each element of the vector corresponds to a physical dimension of the mechanism, and the optimization algorithm will search for the optimal solution within a five-dimensional space. Table 1 presents the value ranges of the structural design variables for the heavy-duty wave compensation platform.

The decision space of the optimization algorithm is constrained within a five-dimensional hyper-rectangular region:

$$\Omega = \{x \in R^5 \mid x_{i,\min} \le x_i \le x_{i,\max}, \tag{2}$$

$$\begin{cases} \mathbf{var}_{\min} = [2000, 3.0, 10, 10, 4.0]^T \\ \mathbf{var}_{\max} = [3000, 4.5, 30, 30, 7.0]^T \end{cases}, \tag{3}$$

where $\mathbf{var}_{\min}$ and $\mathbf{var}_{\max}$ denote the lower and upper bounds of the variables, respectively. These limits are not assigned arbitrarily; rather, they are constrained by practical engineering considerations, such as the available deck space of the

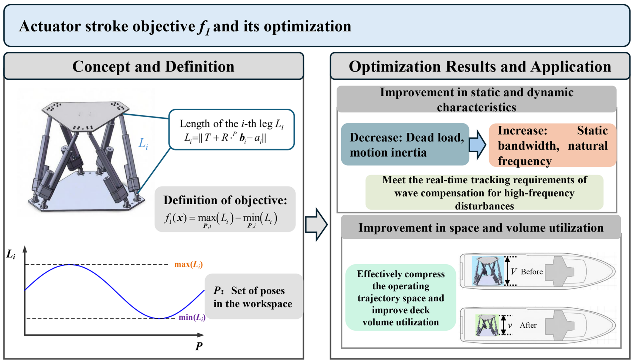

Figure 3. Definition and application of optimization objective f_1.

main vessel, servo-cylinder selection catalogs, and the anti-interference clearance of the joints. Through the parametric description of the geometric configuration of the heavy-duty compensation parallel platform, a design space encompassing the radial dimensions, angular distributions, and spatial height – which characterize the topological features of the mechanism – is established. By setting reasonable physical boundary constraints and proportional constraints, the search process is ensured to be conducted within a set of configurations that satisfy practical engineering requirements.

2.2 Formulation of objective functions

Considering the structural parameters of the heavy-duty compensation parallel platform and practical engineering requirements, the maximum actuator stroke, peak driving force, maximum dexterity, and kinematic isotropy are selected as the four objective functions for the optimization analysis.

2.2.1 (a) Actuator stroke objectivef_1

Minimizing the actuator stroke f_1 yields dual benefits in both structural design and dynamic performance. The definition and application of this optimization objective are illustrated in Fig. 3.

For a given set of poses P in the workspace, which includes the 6-DOF extreme poses, the maximum length of the ith leg, $\max(L_i)$, can be determined through inverse kinematics:

$$L_i = \| \boldsymbol{T} + \mathbf{R} \cdot {}^{\mathrm{P}}\boldsymbol{b}_i - a_i \|, i = 1, \ldots, 6, \tag{4}$$

where $\boldsymbol{T}$ and $\mathbf{R}$ are the translation vector and rotation matrix of the pose transformation, respectively; ${}^{\mathrm{P}}\boldsymbol{b}_i$ represents the coordinates of the moving joint in the moving-coordinate system; and a_i represents the coordinates of the fixed joint in the base coordinate system. The actuator stroke objective f_1 is defined as the difference between the maximum and minimum lengths of the legs within the workspace:

$$f_1(\boldsymbol{x}) = \max_{\boldsymbol{P},i}(L_i) - \min_{\boldsymbol{P},i}(L_i). \tag{5}$$

2.2.2 (b) Peak driving-force objective f_2

The driving-force index is a crucial metric for evaluating the actuation capability of the heavy-duty compensation parallel platform. Its optimization path is illustrated in Fig. 4.

First, the generalized external load vector $\boldsymbol{W}$ is formulated. Considering the total mass M of the moving platform and its payload, along with the diagonal moment of inertia matrix $\mathbf{I}_{\mathrm{b}} = \mathrm{diag}(\boldsymbol{I}_x, \boldsymbol{I}_y, I_z)$, the generalized external load vector $\boldsymbol{W} = [\boldsymbol{F}, \boldsymbol{M}]^T$ applied to the system during dynamic tasks consists of the force component $\boldsymbol{F}$ and the moment component $\boldsymbol{M}$.

Within the force component $\boldsymbol{F}$, the vertical load F_z is the most significant. It comprises the gravitational effect of the total mass of the platform and its payload, the inertial force induced by the motion, and the rated external downward force $F_{\mathrm{ext},z}$, where F_z is expressed as follows:

$$F_z = \boldsymbol{M}(g + a_z) + \left| F_{\mathrm{ext},z} \right|. \tag{6}$$

For the moment component $\boldsymbol{M}$, the rotational moment of inertia of the moving platform, $\mathbf{I}_{\mathrm{b}} = \mathrm{diag}(\boldsymbol{I}_x, \boldsymbol{I}_y, I_z)$, must be taken into account; the inertial moments cannot be neglected during roll or pitch motions. To accurately evaluate the dynamic response of the moving platform during spatial attitude transformations, the generalized moment $\boldsymbol{M}$ is decomposed into the pitch moment $\boldsymbol{M}_x$ about the x axis and the roll moment $\boldsymbol{M}_y$ about the y axis. Combined with the external disturbance moment $\boldsymbol{M}_{\mathrm{ext}}$, the resultant moment is expressed as follows:

$$\begin{cases} \boldsymbol{M}_x = \boldsymbol{I}_x \cdot \epsilon_r + \left| \boldsymbol{M}_{\mathrm{ext},x} \right| \\ \boldsymbol{M}_y = \boldsymbol{I}_y \cdot \epsilon_p + \left| \boldsymbol{M}_{\mathrm{ext},y} \right| \end{cases} \tag{7}$$

where the linear acceleration is $a_z = A_z \cdot \omega^2$, and the angular acceleration is $\alpha_r = A_{\mathrm{rot}} \cdot \omega^2$; A_z and A_{rot} denote the amplitudes of the vertical displacement and the rotation angle, respectively.

Ultimately, the generalized force vector $\boldsymbol{W}$ applied at the center of the moving platform is defined as follows:

$$\boldsymbol{W} = \begin{bmatrix} F_x \\ F_y \\ F_z \\ \boldsymbol{M}_x \\ \boldsymbol{M}_y \\ \boldsymbol{M}_z \end{bmatrix} = \begin{bmatrix} 0 \\ 0 \\ -\left[\boldsymbol{M}(g + a_z) + \left|\boldsymbol{F}_{\mathrm{ext},z}\right|\right] \\ \boldsymbol{I}_x \cdot \alpha_x + \left|\boldsymbol{M}_{\mathrm{ext},x}\right| \\ \boldsymbol{I}_y \cdot \alpha_y + \left|\boldsymbol{M}_{\mathrm{ext},y}\right| \\ 0 \end{bmatrix}. \tag{8}$$

Based on the principle of virtual work, the mapping relationship between the leg driving-force vector $\boldsymbol{F}_{\mathrm{leg}} = [F_1, F_2, F_3, F_4, F_5, F_6]^T$ and the generalized external load $\boldsymbol{W}$ on the moving platform is determined by the force Jacobian matrix $\mathbf{H}$ of the mechanism:

$$\begin{aligned} \boldsymbol{W} &= \mathbf{H} \cdot \boldsymbol{F}_{\mathrm{leg}}, \\ \boldsymbol{F}_{\mathrm{leg}} &= \mathbf{H}^{-1} \boldsymbol{W}, \end{aligned} \tag{9}$$

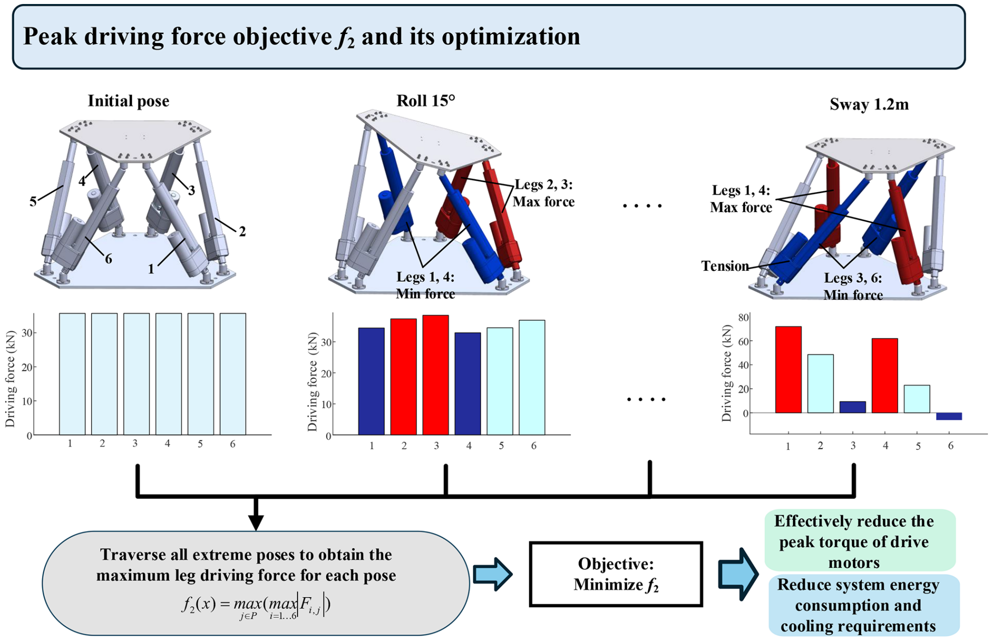

Figure 4. Definition and application of optimization objective f_2.

where each column of $\mathbf{H}$ consists of the unit direction vector $\boldsymbol{n}_i$ of the leg and its moment about the center of the moving platform.

$$\mathbf{H} = \begin{bmatrix} \boldsymbol{n}_1 & \boldsymbol{n}_2 & \boldsymbol{n}_3 & \boldsymbol{n}_4 & \boldsymbol{n}_5 & \boldsymbol{n}_6 \\ \boldsymbol{r}_1 \times \boldsymbol{n}_1 & \boldsymbol{r}_2 \times \boldsymbol{n}_2 & \boldsymbol{r}_3 \times \boldsymbol{n}_3 & \boldsymbol{r}_4 \times \boldsymbol{n}_4 & \boldsymbol{r}_5 \times \boldsymbol{n}_5 & \boldsymbol{r}_6 \times \boldsymbol{n}_6 \end{bmatrix} \quad (10)$$

In the above, $\boldsymbol{r}_i$ denotes the position vector of the ith moving joint with respect to the platform center at the current pose.

A single-dimensional extreme pose traversal method is employed. During the evaluation of each optimization individual, the program examines key poses, including the initial neutral pose and the positive and negative extreme points along the 6-DOF directions. The objective function f_2 extracts the maximum absolute force across all legs under all traversed poses, which is subsequently subjected to magnitude normalization:

$$f_2(x) = \max_{j \in P}(\max_{i=1...6} |F_{i,j}|), \quad (11)$$

where j denotes the traversed pose index, and P represents the set comprising the initial neutral pose and all extreme poses.

2.2.3 (c) Dexterity objective f_3

Formulated based on spatial screw theory and the differential mapping relationship of mechanism kinematics, the Jacobian matrix $\mathbf{J}$ evaluates the mechanism's dexterity, which represents the motion transmission efficiency from the joint space to the task space for the heavy-duty compensation parallel platform:

$$\mathbf{J} = \begin{bmatrix} \boldsymbol{n}_1^T & (\boldsymbol{r}_1 \times \boldsymbol{n}_1)^T \\ \boldsymbol{n}_2^T & (\boldsymbol{r}_2 \times \boldsymbol{n}_2)^T \\ \boldsymbol{n}_3^T & (\boldsymbol{r}_3 \times \boldsymbol{n}_3)^T \\ \boldsymbol{n}_4^T & (\boldsymbol{r}_4 \times \boldsymbol{n}_4)^T \\ \boldsymbol{n}_5^T & (\boldsymbol{r}_5 \times \boldsymbol{n}_5)^T \\ \boldsymbol{n}_6^T & (\boldsymbol{r}_6 \times \boldsymbol{n}_6)^T \end{bmatrix}, \quad (12)$$

where $\boldsymbol{n}_i$ denotes the direction vector of the screw, and $\boldsymbol{r}_i \times \boldsymbol{n}_i$ represents its moment with respect to the moving platform's center. To quantify the omni-directional kinematic transmission performance of the mechanism, the Jacobian matrix is subjected to singular value decomposition:

$$\mathbf{J} = \mathbf{U}\boldsymbol{\Sigma} V^T = \sum_{i=1}^{6} \sigma_i u_i v_i^T, \quad (13)$$

where $\mathbf{V}$ is the orthogonal basis matrix of the joint space (i.e., the leg velocity space); $\mathbf{U}$ is the orthogonal basis matrix of the task space (i.e., the generalized velocity space of the moving platform); and $\boldsymbol{\Sigma} = \mathrm{diag}(\sigma_1, \sigma_2, \sigma_3, \sigma_4, \sigma_5, \sigma_6)$ is the diagonal matrix of singular values, with its elements satisfying $\sigma_1 \geq \sigma_2 \geq \sigma_3 \geq \sigma_4 \geq \sigma_5 \geq \sigma_6 \geq 0$.

According to the geometric interpretation of singular value decomposition (SVD), if the actuation velocities of the six legs are constrained within a unit hypersphere, this unit sphere is mapped by the Jacobian matrix into a six-dimensional kinematic manipulability ellipsoid in the task space. The value σ_6, namely $\sigma_{\min}$, defines the length of the shortest semi-axis of this motion transmission ellipsoid. As

$\sigma_{\min} \to 0$, the ellipsoid degenerates into a lower-dimensional geometry, indicating that $\det(J) \to 0$ and the mechanism approaches a singular configuration. A larger $\sigma_{\min}$ implies that the mechanism can still maintain a favorable kinematic response even in the least performant direction.

By maximizing this minimum singular value, the shortest semi-axis of the kinematic manipulability ellipsoid can be effectively expanded. The objective function f_3 is defined as follows:

$$f_3(x) = -\min_{j \in p} \left(\sigma_6(\mathbf{J}_j)\right). \tag{14}$$

2.2.4 (d) Isotropy objective f_4

Isotropy reflects the uniformity of the kinematic performance of the heavy-duty compensation parallel platform within the 6-DOF space. Based on the aforementioned singular SVD of the Jacobian matrix $\mathbf{J}$, the condition number κ of the mechanism at a specific pose is defined as the ratio of its maximum singular value to its minimum singular value:

$$\kappa(\mathbf{J}) = \frac{\sigma_{\max}(\mathbf{J})}{\sigma_{\min}(\mathbf{J})} = \frac{\sigma_1}{\sigma_6}, \tag{15}$$

where $\boldsymbol{\kappa} \in [1, +\infty)$. The condition number κ serves as an index measuring the degree of disparity of the matrix. When $\kappa = 1$, the kinematic manipulability ellipsoid transforms into a perfect hypersphere, implying that a unit velocity input in the leg joint space generates a completely consistent response in all directions within the task space. At this point, the mechanism achieves an ideal state of velocity isotropy.

The maximum condition number within the traversed pose set P is selected as the optimization objective. By minimizing this index, the performance fluctuations of the mechanism at extreme poses can be effectively suppressed. The objective function f_4 is defined as follows:

$$f_4(x) = \max_{j \in P} \left(\boldsymbol{\kappa}(\mathbf{J}_j)\right). \tag{16}$$

3 Construction of ANN-based performance surrogate model

To balance the computational accuracy and search efficiency during the optimization of the heavy-duty compensation parallel platform, an ANN is introduced to construct a physical performance surrogate model.

3.1 Sample space sampling and objective value normalization

The accuracy of the surrogate model is highly dependent on the distribution quality of the training samples within the design space. In this study, all 2500 datasets were numerically generated using a customized physical simulation program developed in MATLAB. Specifically, the input parameters were generated via a random sampling function within the structural design boundaries. The corresponding multi-physics output responses were subsequently calculated using MATLAB's mathematical solvers: the actuator stroke was solved via spatial inverse kinematics, the peak driving force was derived using the virtual work principle via the force Jacobian matrix, and the dexterity and isotropy indices were quantified using SVD. To address the issue of magnitude disparity among different performance objectives of the heavy-duty compensation parallel platform – for instance, the actuation stroke objective f_1 is at the 10^0 order of magnitude, whereas the peak driving-force objective f_2 is at the 10^5 order of magnitude – Z-score standardization is applied to the output objective vectors. This ensures that the neural network can evenly capture the features of various physical domains during the training process:

$$\hat{y}_{i,j} = \frac{y_{i,j} - \mu_j}{\sigma_j}, \tag{17}$$

where $y_{i,j}$ is the true value of the jth objective for the ith sample, and μ_j and are σ_j the sample mean and standard deviation of this objective, respectively.

3.2 Neural network topology and training

A deep neural network model with a four-layer structure is established, with its overall architecture defined as 5-20-15-4. The input layer corresponds to five structural decision variables, and the two hidden layers contain 20 and 15 neurons, respectively, employing sigmoid activation functions to capture highly nonlinear mapping relationships; the output layer corresponds to four standardized performance metrics. Through the nonlinear transformation of the dual hidden layers, high-speed prediction of four performance objectives – actuator stroke, driving force, dexterity, and isotropy – is ultimately achieved at the output layer.

The number of hidden layers and neurons in the artificial neural network was determined through a systematic grid search and trial-and-error approach, aiming to balance predictive accuracy and computational efficiency. Initially, empirical formulas were utilized to define the approximate range of the number of neurons. Subsequently, various network models containing one to three hidden layers with different neuron combinations were trained and evaluated. The evaluation results indicated that a single hidden layer lacked the capacity to accurately map the highly nonlinear multi-physics responses of the 6-DOF platform, whereas a three-hidden-layer architecture was highly prone to overfitting and consumed excessive training time. Through performance comparison on the validation set, the dual-hidden-layer architecture containing 20 and 15 neurons, respectively, demonstrated the most robust generalization capability. Consequently, a deep neural network model with an overall architecture defined as 5-20-15-4 was ultimately established.

The training process employs the Levenberg–Marquardt algorithm, which features a second-order convergence rate.

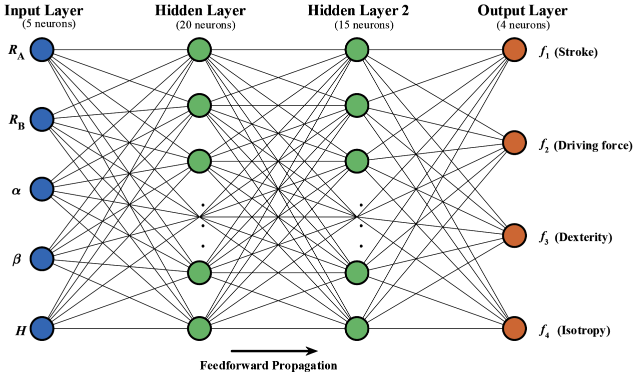

Figure 5. ANN surrogate model architecture.

Its weight update formula is given by the following:

$$w_{k+1} = w_k - [\mathbf{J}_t^T \mathbf{J}_t + \mu I]^{-1} \mathbf{J}_t^T e, \tag{18}$$

where $\mathbf{J}_t$ is the Jacobian matrix of the error with respect to the weights, μ is the damping factor, and e is the training error.

3.3 Accuracy assessment of the surrogate model

The goodness of fit is employed to independently evaluate the four performance objectives. The calculation formula is as follows:

$$R^2 = 1 - \frac{\sum_{i=1}^{\mathrm{n}} \left(y_i - \hat{y}_i\right)^2}{\sum_{i=1}^{\mathrm{n}} (y_i - \bar{y}_i)^2}, \tag{19}$$

where y_i is the true value from the physical simulation, and $\hat{y}_i$ is the predicted value from the neural network.

The 2500 sets of sampled data are divided into a training set and a testing set at a ratio of 8 : 2. To eliminate potential data error risks and ensure the training reliability of the ANN, it is necessary to clarify that these 2500 datasets are not empirical measurements susceptible to observation noise but exact numerical solutions strictly generated from closed-form analytical equations such as spatial inverse kinematics and the virtual work principle. Furthermore, the numerical solver was systematically pre-verified under typical boundary conditions prior to the bulk generation to guarantee the physical credibility of the datasets. The regression analysis results of the surrogate model on the independent testing set are shown in Fig. 6, where the horizontal axis represents the true values from the physical simulation, and the vertical axis represents the predicted outputs of the neural network surrogate model. The average R^2 values of all objectives reach over 0.98, demonstrating that the constructed ANN surrogate model possesses high fitting accuracy across the entire variable space, thereby satisfying the performance evaluation requirements for the subsequent NSGA-III optimization.

Furthermore, a 0.5 % level of Gaussian white noise was introduced into the training data. This operation is designed to simulate the stochastic response of the heavy-duty compensation parallel platform under uncertainties such as manufacturing errors, joint clearances, and sensor measurement noise. The experimental results demonstrate that the R^2 values of the noise-injected surrogate model on the independent testing set remain between 0.987 and 0.999.

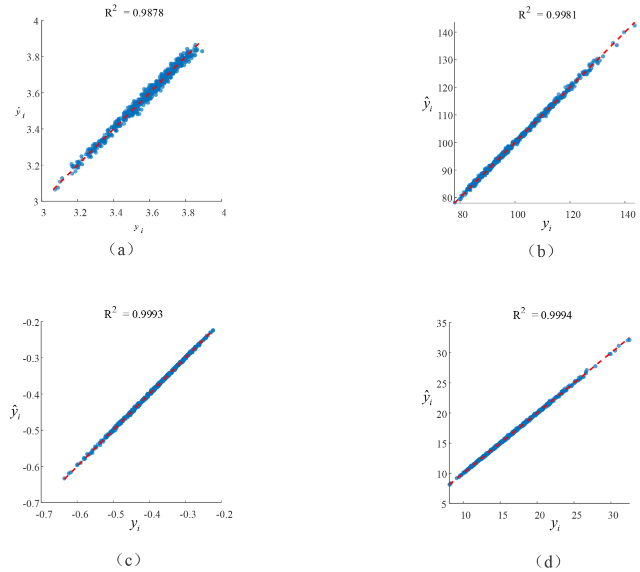

Figure 6. Average R^2 values for each objective. **(a)** Objective function f_1. **(b)** Objective function f_2. **(c)** Objective function f_3. **(d)** Objective function f_4.

4 Design of the improved NSGA-III optimization algorithm

To address the conflicting multi-objective optimization problem of the heavy-duty compensation parallel platform, an improved NSGA-III algorithm is introduced. While the standard NSGA-III is inherently well-suited for high-dimensional spaces via its reference-point mechanism, specific algorithmic improvements were implemented to adapt to the physical complexities of the platform. These improvements primarily include (1) integrating a dynamic objective space normalization strategy to eliminate extreme order-of-magnitude biases among different physical domains and (2) embedding a feasibility-rule-based constraint violation degree, CV(x), into the evolutionary selection phase to strictly penalize geometric interferences and singularities. By guiding the population evolution through predefined uniform reference points on a hyperplane, it accurately captures the high-dimensional Pareto front while guaranteeing convergence.

4.1 Reference point construction and objective space normalization

The diversity maintenance mechanism of NSGA-III is based on a reference point network. A systematic projection method is employed to construct hyperplane reference points within the objective space. For a task with M objectives and p divisions, the total number of reference points $\boldsymbol{N}_{\mathrm{ref}}$ follows the combinatorial relationship below:

$$\boldsymbol{N}_{\mathrm{ref}} = \begin{pmatrix} M+p-1 \\ p \end{pmatrix}. \tag{20}$$

With the number of divisions set to $p = 12$, a total of 455 uniformly distributed reference vectors are generated within the four-dimensional objective space. Given the significant order-of-magnitude disparities among the physical metrics of the heavy-duty compensation parallel platform – for instance, the actuation stroke metric f_1 is at the 10^0 scale, whereas the peak driving-force metric f_2 is at the 10^5 scale – the algorithm performs a normalization process in each evolutionary generation to eliminate scale bias. First, the ideal point $\mathbf{z}^* = (z_1^*, z_2^*, \ldots, z_M^*)$ is determined based on the minimum values of the population. Subsequently, the extreme points are identified by minimizing a scalarizing function to construct a hyperplane. The j-th objective function value $f_{i,j}$ of individual i is then mapped into the normalized interval:

$$f'_{i,j} = \frac{f_{i,j} - z_j^*}{a_j - z_j^*}, \tag{21}$$

where a_j is the intercept of the hyperplane with the jth objective axis. This process ensures that the search process takes place within a unit simplex, thereby assigning equal evolutionary weights to all performance metrics.

4.2 Genetic operator design and constraint violation handling

The algorithm employs real-coded simulated binary crossover and polynomial mutation to generate superior offspring configurations. Before calculating the overall violation degree, two specific geometric interference criteria are explicitly defined: the dynamic actuator length l_i must satisfy the physical stroke limits, i.e., $l_{\min} \le l_i \le l_{\max}$, and the spatial deflection angle θ_i must not exceed the maximum allowable cone angle of the Hooke's joints, i.e., $\theta_i \le \theta_{\max}$. Exceedances of these physical boundaries are directly transformed into specific interference constraint functions $g_k(x)$. Furthermore, to address the complex interference and singularity constraints of the platform, a handling logic based on feasibility rules is introduced. The overall constraint violation degree $\mathrm{CV}(x)$ of individual x is defined as the weighted sum of individual constraint violations:

$$\mathrm{CV}(x) = \sum_{k=1}^{m} \max(0, g_k(x)). \tag{22}$$

During the parent selection phase, the algorithm adheres to the following rules: if both individuals are feasible, they are selected based on their non-domination ranks; if infeasible individuals are involved, the one with the smaller CV value is preferentially retained.

4.3 Niche preservation and environmental selection mechanism

During the environmental selection phase, NSGA-III maintains the population distribution by calculating the perpendicular distance between individuals and reference lines, which replaces the crowding distance used in traditional algorithms. For an individual s and a reference line w in the normalized space, their perpendicular distance $d(s, w)$ is expressed as follows:

$$d(s, w) = \left\| (f'(s) - z^*) - \frac{(f'(s) - z^*)^T w}{\|w\|} w \right\|. \tag{23}$$

Based on a niche counting mechanism, the algorithm preferentially retains solutions around the reference points that have the fewest associated individuals. This dynamic screening strategy forces the population to be uniformly distributed across the four-dimensional Pareto front, thereby excavating potential optimal configurations.

5 Comparative analysis of optimization results

By setting the number of reference point divisions H_{div} to 12, a total of 455 uniformly distributed reference point directions are generated. The population size N_{pop} is set to 455 to match the number of reference points, thereby enhancing the algorithm's niche preservation capability in the multi-dimensional objective space. The maximum number of evolutionary iterations is set to 120 to ensure sufficient convergence of the solution set. Furthermore, the crossover probability P_{c} is set to 0.9 to maintain the recombination rate of superior genes, and the mutation probability P_{m} is set to 0.15 to guarantee that the algorithm possesses adequate random perturbation capability.

By integrating 3D scatter coordinate mapping with a 4D color map, four complementary sets of 4D performance space distribution plots are constructed, as shown in Fig. 7.

The 455 sets of Pareto optimal solutions ultimately obtained exhibit the competitive trade-off relationships among different objectives. Accordingly, three typical design domains are summarized: (1) a compact scheme suitable for limited deck space, with an actuation stroke of less than 3500 mm and a height of less than 4700 mm; (2) a robust scheme suitable for heavy loads, featuring a base platform radius of approximately 4000 mm and a height of around 6150 mm; and (3) a dexterous scheme prioritizing kinematic performance, with a dexterity greater than 0.44 and a condition number of less than 14.3.

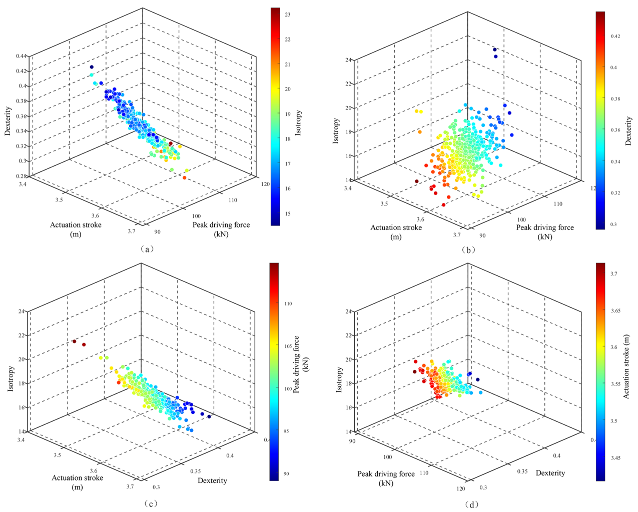

Figure 7. Visualization of the 3D Pareto front. **(a)** Optimization objective combination 1. **(b)** Optimization objective combination 2. **(c)** Optimization objective combination 3. **(d)** Optimization objective combination 4.

5.1 Comprehensive evaluation and comparative analysis of multi-objective optimization results

Figure 8 illustrates the sensitivity correlation characteristics between the structural parameters and the objective functions.

Figure 8 reveals the sensitivity patterns of each structural parameter on the system performance. The global sensitivity indices follow the order of $R_B > H > R_A > \beta > \alpha$. Among them, the upper-platform radius R_B is the most critical variable; increasing R_B can reduce the peak load and improve kinematic dexterity. The initial height H dominates the actuation stroke; an excessive height will lead to a sharp increase in the telescoping span and deteriorate the isotropy. Appropriately increasing the base platform radius R_A helps mitigate stroke redundancy.

Taking the structural parameter R_B as a vital characteristic parameter for further analysis, variations in the value of R_B can simultaneously influence three optimization objectives. Within different parameter intervals, the interactive relationships among these optimization objectives may vary, as illustrated in Fig. 9.

As shown in Fig. 9, increasing R_B can significantly optimize the force mapping to evenly distribute the load; as it increases from 2140 to 3110 mm, the peak driving force decreases from 117.47 to 87.44 kN. In terms of kinematics, R_B enhances the mechanism dexterity with a correlation coefficient of $r = 0.843$. Meanwhile, it exhibits a strong negative correlation with the condition number ($r = -0.774$), which drops substantially from approximately 22 to 14.28.

5.2 Result screening and comprehensive evaluation

Based on the sensitivity correlations between the design variables and the performance objectives, the 455 non-dominated solutions obtained via optimization are compared against the baseline of initial structural parameters. This comparison aims to screen out the optimized solutions that exhibit improvements across three to four optimization objectives. Figure 10 illustrates the performance enhancements of the 91 selected optimal solutions relative to the initial structural baseline.

The analysis indicates that the improvements in dexterity and peak driving force are the most prominent. Across the entire solution set, dexterity increases by 1 % to 20 %, with solution 1 reaching 18.88 %. The peak driving force decreases by 8 % to 14 %, and, notably, solution 3 drops from 103.11 to 90.97 kN. Constrained by the relatively optimal initial baseline, the stroke reduction rate remains stable between 1 % and 5 %.

5.2.1 Construction and positivation of the decision evaluation matrix

The decision matrix serves as the quantitative foundation for multi-criteria decision analysis. After non-dominated sorting and preliminary screening, 91 representative Pareto optimal solutions are obtained to form a candidate scheme set $S = S_1, S_2, S_3,..,S_{91}$. Each scheme is characterized by four performance objective metrics. The original decision matrix $\mathbf{X}$ is constructed as follows:

$$\mathbf{X} = \begin{bmatrix} x_{11} & x_{12} & x_{13} & x_{14} \\ x_{21} & x_{22} & x_{23} & x_{24} \\ \vdots & \vdots & \vdots & \vdots \\ x_{n1} & x_{n2} & x_{n3} & x_{n4} \end{bmatrix}, \tag{24}$$

where the rows of the matrix represent different configuration schemes, and the columns represent the four performance metrics. The first column ($j = 1$) denotes the actuation stroke f_1, the second column ($j = 2$) denotes the peak driving force f_2, the third column ($j = 3$) denotes the mechanism dexterity f_3, and the fourth column ($j = 4$) denotes the isotropy f_4.

In the comprehensive system performance evaluation, the optimization directions of the evaluation metrics vary. To facilitate a unified weighted calculation, the metrics must undergo a positivation classification process. Specifically, the actuation stroke f_1, peak driving force f_2, and condition number f_4 are cost-type metrics that are considered optimal when minimized. Conversely, the mechanism dexterity f_3 is a benefit-type metric that is considered optimal when maximized. For the cost-type metrics, the positivation transformation formula is

$$x'_{ij} = \max(x_{ij}) - x_{ij}, \tag{25}$$

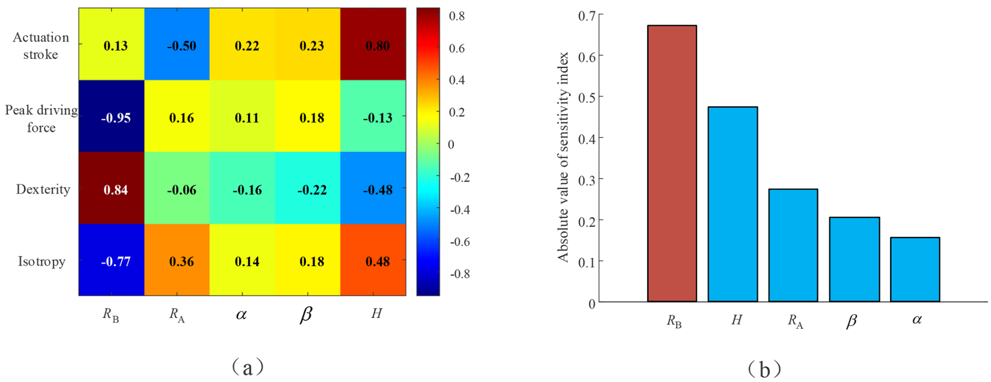

Figure 8. Sensitivity relationship between structural parameters and objective functions. **(a)** Linear correlation heatmap. **(b)** Influence ranking of structural parameters on performance.

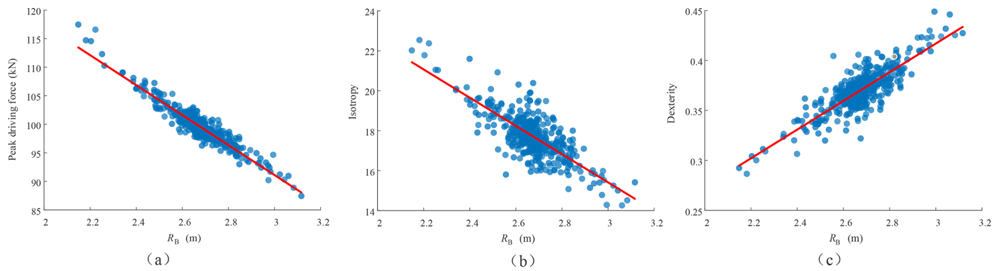

Figure 9. Sensitivity relationship between structural parameters and objective functions. **(a)** RB vs. peak driving force. **(b)** RB vs. dexterity. **(c)** RB vs. Isotropy.

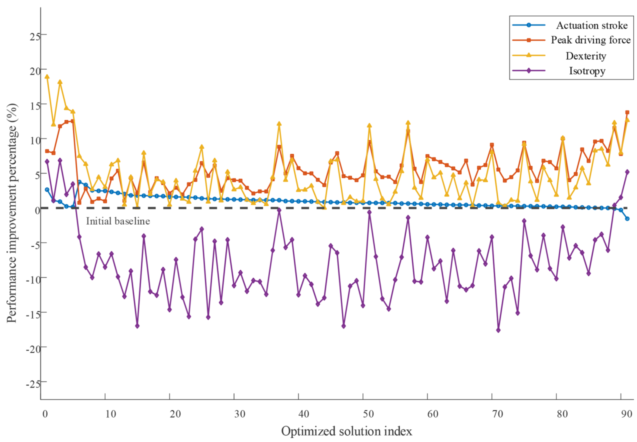

Figure 10. Line chart of performance improvement percentages.

where $\max(x_{ij})$ is the maximum value of the jth metric across all candidate schemes. For the benefit-type metrics, their original values remain unchanged:

$$x'_{ij} = x_{ij}. \tag{26}$$

After executing the above procedure, the original matrix **X** is transformed into the positivated decision matrix **X'**. At this point, all numerical values within the columns of the matrix exhibit the property where larger values indicate better performance.

$$r_{ij} = \frac{x'_{ij}}{\sqrt{\sum_{i=1}^{n}\left(x'_{ij}\right)^2}}. \tag{27}$$

In the configuration selection of the heavy-load compensation parallel mechanism, the contributions of different performance metrics to mission success are not equal. Based on the previous sensitivity analysis results of the structural parameters and combined with practical requirements, a weighted scoring mechanism is adopted. The weight vector is defined as follows:

$$\boldsymbol{w} = [w_1, w_2, w_3, w_4]^T. \tag{28}$$

According to practical engineering needs, different weight coefficients are assigned to various optimization objectives. Emphasizing the constraints of installation space and extension length, the weight of the actuation stroke is set to $w_1 = 0.25$. Since the wave compensation mechanism involves heavy-load operations, the peak driving force directly determines the safety of the drive system and is therefore assigned the highest weight of $w_2 = 0.30$. Meanwhile, the weight of the mechanism dexterity is set to $w_3 = 0.25$, and the weight of the condition number is set to $w_4 = 0.20$.

Applying the aforementioned weight vector to the normalized matrix **R** yields the weighted normalized decision matrix $\mathbf{V} = (v_{ij})_{n\times m}$. Each element in this matrix represents the contribution score of the scheme for a specific metric:

$$v_{ij} = w_j \cdot r_{ij}. \tag{29}$$

By introducing the weight coefficients, the weighted matrix **V** modifies the geometric morphology of the performance space. In the subsequent calculation of distances to the ideal solutions, the coordinate axes corresponding to metrics with larger weights are proportionally stretched in the Euclidean space. Consequently, schemes that excel in the core metrics are more likely to stand out in the final ranking.

5.2.2 Determination of positive and negative ideal solutions and calculation of Euclidean distances

Within the weighted performance space, the positive ideal solution is a virtual optimal scheme where each metric takes the maximum value from the corresponding metrics in the candidate solution set. The negative ideal solution is a virtual scheme composed of the minimum values of each metric. Since the metrics have undergone the positivation process in the previous section, all metric columns now exhibit the larger-the-better characteristic. Therefore, the coordinates of the positive and negative ideal solutions are determined by the following formulas:

$$\begin{cases} A^+ & = \left(v_1^+, v_2^+, v_3^+, v_4^+\right) \\ & = \left(\max_i v_{i1} \max_i v_{i2}, \max_i v_{i3}, \max_i v_{i4}\right) \\ A^- & = \left(v_1^-, v_2^-, v_3^-, v_4^-\right) \\ & = \left(\min_i v_{i1}, \min_i v_{i2}, \min_i v_{i3}, \min_i v_{i4}\right) \end{cases}, \tag{30}$$

where $i \in \{1, 2, 3, \ldots, 91\}$ denotes the index of the 91 schemes, and v_{ij} is the weighted normalized value of the ith scheme on the jth metric. The positive ideal solution component v_j^+ represents the weighted upper bound of the jth metric among all schemes, indicating the optimal performance. The negative ideal solution component v_j^- represents the lower bound of the performance bottleneck allowed for the jth metric. After executing this step, the originally abstract 91 sets of solutions are successfully placed within a hyper-rectangular performance interval defined by A^+ and A^-, providing a reasonable reference for the final comprehensive scoring.

5.2.3 Calculation of relative closeness and final scheme selection

The relative closeness coefficient C_i is defined as the final evaluation metric to measure the superiority of the 6-DOF wave compensation platform configurations. Its calculation formula is as follows:

$$C_i = \frac{D_i^-}{D_i^+ + D_i^-}, \tag{31}$$

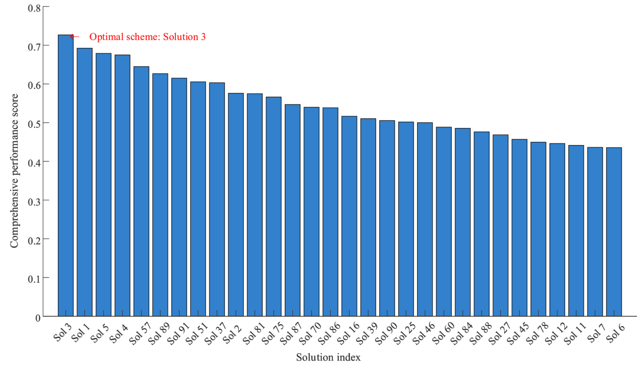

Figure 11. Bar chart of the comprehensive performance ranking of the solution set.

where$i$ =1,2,3,...,91; D_i^+ is the Euclidean distance from the ith scheme to the positive ideal solution, and D_i^- is the Euclidean distance from the ith scheme to the negative ideal solution. The value of the relative closeness C_i is strictly bounded within the interval [0,1], and its magnitude reflects the comprehensive competitiveness of the scheme represented by the optimized solution. When it approaches 1, it indicates that the scheme is closer to the positive ideal solution and further from the negative ideal solution. If $C_i = 1$, it implies that the scheme has reached the extreme level of the Pareto front across all performance dimensions. When it approaches 0, it signifies that the scheme has almost hit the lower bounds of all performance metrics, classifying it as the worst configuration.

Based on the C_i index, the 91 optimized solutions are sorted in descending order to construct an optimal decision sequence. The top-ranked scheme is thus locked in as the global optimal configuration. This closeness-based screening logic possesses a decision-making advantage: it evaluates the excellence of a scheme not only by determining its proximity to A^+ but by simultaneously assessing the stability of the scheme by determining its distance from A^-.

As shown in Fig. 11, [Sol 3] is identified as the final recommended scheme through comprehensive scoring, and it occupies a central and balanced position on the Pareto front.

Figure 12 demonstrates that the mechanism dexterity of the optimal solution surges by 18.12 %, the isotropy improves by 6.85 %, the peak driving force decreases by 11.78 %, and the actuation stroke is reduced by 0.92 %. In summary, while ensuring structural compactness, this optimal configuration significantly enhances motion transmission efficiency and alleviates the actuator load.

5.3 Multi-objective performance comparison between the improved and traditional algorithms

In this section, the traditional NSGA-II algorithm is selected as the classical baseline for comparison. Rather than treating it as a competing meta-optimizer, NSGA-II is strictly

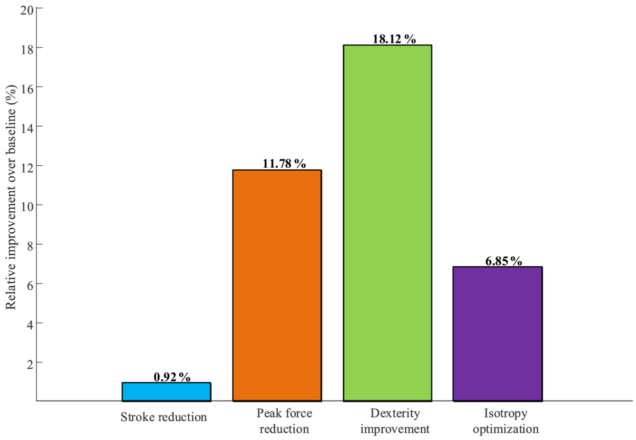

Figure 12. Comprehensive performance gains of the optimal solution.

employed as a control group to demonstrate the exact limitations of the traditional crowding-distance mechanism in a four-objective space, thereby highlighting the necessity and performance leap brought by the reference-point mechanism of NSGA-III. Three core evaluation metrics in the multi-objective optimization field are introduced to conduct a quantitative comparative analysis of the optimized solution sets from the traditional NSGA-II algorithm and the enhanced multi-objective genetic algorithm NSGA-III. The spacing metric SP is utilized to measure the distribution uniformity of the non-dominated solution set. Its calculation formula is as follows:

$$\mathrm{SP}=\sqrt{\frac{1}{n-1}\sum_{i=1}^{n}\left(\overline{d}-d_i\right)^2}, \tag{32}$$

where n is the total number of obtained non-dominated solutions, and d_i is the minimum Euclidean distance from the ith solution to the other solutions in the set, expressed as

$$d_i=\min_{j\in\{1,2,\ldots,n\},j\neq i}\left(\sum_{k=1}^{M}\|f_k^i-f_k^j\|_2\right), \tag{33}$$

$$\overline{d}=\frac{1}{n}\sum\nolimits_{i=1}^{n}d_i, \tag{34}$$

where M is the number of objective functions, and $\overline{d}$ is the average of all minimum distances d_i. Numerically, the SP metric reflects the standard deviation of individual spacing on the Pareto front. When $\mathrm{SP}=0$, it indicates that all non-dominated solutions are arranged at completely equal intervals in the objective space, reaching an ideal uniform state. A smaller SP value signifies that the distribution of the solution set tends to be more uniform, and the algorithm's ability to capture the performance front is more stable, without obvious performance gaps or individual crowding phenomena.

Table 2. Comparison of evaluation metrics.

Evaluation metric	NSGA-II	NSGA-III
SP	0.0794	0.0497
MS	1.8616	1.6211
HV	0.8721	1.1010

The maximum spread metric MS is used to evaluate the algorithm's exploration capability regarding the extreme boundaries of the objective space. Its formula is defined as the Euclidean distance between the two furthest solutions in the normalized objective space:

$$\mathrm{MS}=\max_{i,j\in\{1,2,\ldots,N\}}\sqrt{\sum_{m=1}^{M}\left(f_m^{(i)}-f_m^{(j)}\right)^2}, \tag{35}$$

where M is the objective dimension, and $f_m^{(i)}$ is the normalized value of the ith solution on the mth objective. A larger MS value indicates that the algorithm has a wider coverage range over the extreme parameter boundaries.

The comprehensive hypervolume indicator HV is an important metric for evaluating the comprehensive performance of multi-objective optimization algorithms, taking into account both convergence and diversity. Let the reference point be $\boldsymbol{r}=[r_1,r_2,\ldots,r_M]^T$. HV is defined as the hypergeometric volume enclosed by the Pareto solution set and the reference point in the objective space:

$$\mathrm{HV}=\mathrm{Volume}\left(\bigcup_{i=1}^{N}\left[f_1^{(i)},r_1\right]\times\ldots\times\left[f_m^{(i)},r_m\right]\right). \tag{36}$$

A larger HV value indicates that the solution set generated by the algorithm is closer to the true perfect front and covers a broader trade-off space, reflecting superior overall multi-objective performance. After applying range normalization to the optimization results of NSGA-II and NSGA-III, the statistical results of the above three metrics are calculated, and these are presented in Table 2:

The analysis shows that its SP value drops to 0.0497, representing a decrease of 37.4 %, and the HV value increases by 26.2 %. Although the MS value of NSGA-III is slightly lower than that of NSGA-II, it eliminates the artificial inflation of MS caused by isolated extreme solutions in the traditional algorithm. NSGA-III generates an internally highly continuous solution set, which holds greater significance for engineering guidance. The comparison of structural parameters before and after optimization is shown in Table 3.

Through comparison, it is evident that the improved NSGA-III algorithm benefits from the introduction of a dynamic penalty mechanism for physical interference. Its optimal scheme not only reasonably expands the base support span of the platform – with R_A increasing to 3881 mm

Table 3. Comparison of structural parameters and performance metrics before and after optimization.

Structural parameter	Initial baseline	NSGA-II	NSGA-III
R_B (mm)	2500	2083	3060
R_A (mm)	3500	3011	3881
α (°)	20	10.65	19.82
β (°)	20	10.99	19.04
H (mm)	5000	5781	5291

Table 4. Comparison of optimization metrics before and after optimization.

Optimization metric	Initial baseline	NSGA-II	NSGA-III
f_1 (mm)	3601	3692	3567
f_2 (kN)	103.11	98.24	90.97
f_3	0.3776	0.4372	0.4460
f_4	15.31	11.14	14.26

and R_B increasing to 3060 mm, coupled with a height of 5291 mm to enhance overall stiffness and force performance – but also stably maintains α and β at 19.82 and 19.04°. This result closely aligns with the initial design of 20°, ensuring a safe installation clearance for the hinges. The comparison of the four optimization metrics between NSGA-II and NSGA-III is presented in Table 4.

Table 4 indicates that the comprehensive performance of the improved NSGA-III is superior to that of NSGA-II. By relying on mechanisms such as dynamic normalization to escape local optima, it successfully reduces the peak driving force to 90.97 kN, increases the dexterity to 0.4460, and optimizes the actuation stroke to 3567 mm. Although its condition number of 14.26 superficially appears to be inferior to the 11.14 of the latter, this is actually the optimal solution derived from a multi-dimensional trade-off after strictly avoiding the boundaries of mechanical interference and introducing the penalty mechanism, rather than a degradation in performance.

5.4 Prototype development and physical validation

A proof-of-concept prototype of the wave compensation parallel platform was developed. This prototype employs DC linear actuators as the underlying actuation units, and its core geometric parameters are designed as follows: the radius of the upper platform hinge point circle R_B is 180 mm, the radius of the lower platform hinge point circle R_A is 260 mm, and the initial neutral posture height H is 370 mm. According to the optimization results, the angles between the hinge points of the upper and lower platforms, $\alpha$and β, are 19.82 and 19.04°, respectively. Based on this prototype, dynamic tests of extreme postures were conducted. The upper platform executed roll-and-pitch extreme posture commands with an amplitude of ±15°, respectively, as shown in Fig. 13.

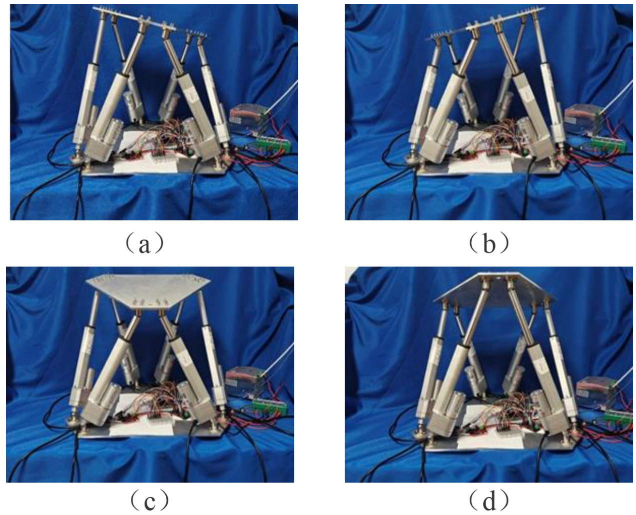

Figure 13. Motion experiment of the prototype. **(a)** Roll 15°. **(b)** Roll −15°. **(c)** Pitch 15°. **(d)** Pitch −15°.

To comprehensively evaluate the reliability of the optimized configuration, the extreme posture experiment was consecutively repeated 50 times. Furthermore, a quantitative comparison between the optimized theoretical results and the physical experimental data was performed. The measurement results indicated that the relative error between the theoretical target angles and the actual executed angles of the prototype remained strictly within 1 % across all test cycles. The experimental results demonstrate that the six straight legs of the platform operate smoothly throughout the 50 consecutive cycles, with no physical collisions or interference occurring between the kinematic pairs and the connecting links.

6 Conclusions

This paper employs an ANN surrogate model to characterize the complex mapping relationships between topological parameters and physical performance metrics. A multi-objective optimization mathematical model linking structural dimensions to the kinematic and dynamic performance of a heavy-duty parallel platform is established. The optimal structural configuration is determined using an improved NSGA-III algorithm combined with the TOPSIS method, thereby providing an efficient and feasible engineering solution for the prototype development of wave compensation equipment. Key conclusions are as follows:

1. To address the multi-parameter coupling and complex solving issues in the optimal design of the heavy-load compensation parallel platform, an artificial neural net-

work is introduced to construct an explicit surrogate model, achieving an order-of-magnitude leap in computational efficiency. By employing an improved NSGA-III algorithm enhanced with a reference point mechanism and an interference penalty strategy, the drawbacks of solution set crowding and pseudo-optimal solutions involving mechanical interference are successfully overcome. Quantitative comparisons reveal that the SP and HV metrics of the improved algorithm are enhanced by 37.4 % and 26.2 %, respectively, compared to those of NSGA-II.

2. The analysis indicates that the upper platform radius R_B and the initial height H are the core characteristic parameters dictating the comprehensive performance of the system. Specifically, H directly dominates the actuation stroke and the static spatial envelope. Meanwhile, appropriately increasing R_B can significantly optimize the force mapping to reduce peak loads and substantially boost motion transmission efficiency. Prioritizing the regulation of these two parameters serves as a key strategy for achieving an optimal trade-off among structural compactness, low actuation power consumption, and high dexterity in the heavy-load compensation parallel platform.

3. Utilizing the TOPSIS method, the global optimal configuration is successfully identified. Compared to the initial baseline, the optimal scheme achieves an 18.12 % increase in dexterity, an 11.78 % reduction in peak driving force, and a 6.85 % optimization in the condition number, all while reducing the actuation stroke by 0.92 %. This result effectively reconciles the conflicts among multiple physical metrics of the heavy-load compensation parallel platform, realizing Pareto improvements and global synergy in the comprehensive system performance. This research provides a reliable design benchmark for the prototype development of wave compensation equipment.

7 Limitations and future works

Although the proposed multi-objective optimization method successfully improves the topological parameters of the heavy-duty parallel platform, this study still has certain limitations. The current dynamic evaluation primarily relies on rigid-body assumptions. For a 20 t class wave compensation system, the structural flexibility and elastic deformation of the mechanism under extreme dynamic loads have not been fully captured, which may affect the ultimate compensation precision slightly. Furthermore, this optimization focuses on the structural configuration independent of the control strategy. Therefore, future research will focus on developing a multibody dynamics model to investigate the impact of structural deformation and further exploring control structure co-design to evaluate the platform's real-time dynamic tracking performance under actual stochastic wave spectrum disturbances.

Data availability. No data sets were used in this article.

Author contributions. Methodology: T. Z. H.; software: R. J. L.; investigation: L. F. M. and J. W.; writing (original draft preparation): G. X. Z.; writing (review and editing): F. Z. All of the authors have read and agreed to the published version of the paper.

Competing interests. The contact author has declared that none of the authors has any competing interests.

Disclaimer. Publisher's note: Copernicus Publications remains neutral with regard to jurisdictional claims made in the text, published maps, institutional affiliations, or any other geographical representation in this paper. The authors bear the ultimate responsibility for providing appropriate place names. Views expressed in the text are those of the authors and do not necessarily reflect the views of the publisher.

Financial support. This research was funded by the Special Innovation Fund Project for University Cooperation of Shanghai Marine Equipment Research Institute (GX-Self-funded-Research-Institute-25Z008), the Natural Science Foundation of the Jiangsu Higher Education Institutions of China (grant no. 23KJB460010), the Science and Technology Plan Project of Wenzhou Municipality (grant no. G20240076), and the Zhejiang College of Security Technology School-Level Key Project (grant no. AF2025Z05).

Review statement. This paper was edited by Pengyuan Zhao and reviewed by Thanh-Phong Dao and one anonymous referee.

References

Abdur, R., Bashar, E., and Anas, A.: Genetic and hybrid algorithms for optimization of non-singular 3PRR planar parallel kinematics mechanism for machining application, Robotica, 36, 839–864, https://doi.org/10.1017/S0263574718000152, 2018.

Bhosekar, A. and Ierapetritou, M.: Advances in surrogate based modeling, feasibility analysis, and optimization: A review, Comput. Chem. Eng., 108, 250–267, https://doi.org/10.1016/j.compchemeng.2017.09.017, 2018.

Briot, S. and Khalil, W.: Dynamics of parallel robots: From rigid bodies to flexible elements, Springer, https://doi.org/10.1007/978-3-319-19788-3, 2015.

Chen, W., Wen, Y., Tong, X., Lin, C., Li, Jiang., Wang, S., Xie, W., Mao, L., Zhao, X., Zhang, W., and Gao, F.: Dynamics modeling and modal space control strategy of ship-borne Stewart platform for wave compensation, J. Mech. Robot., 15, 041015, https://doi.org/10.1115/1.4062177, 2023.

Chugh, T., Sindhya, K., Hakanen, J., and Miettinen, K.: A survey on handling computationally expensive multiobjective optimization problems with evolutionary algorithms, Soft Comput., 23, 3137–3166, https://doi.org/10.1007/s00500-017-2965-0, 2017.

Dasgupta, B. and Mruthyunjaya, T.: The Stewart platform manipulator: A review, Mech. Mach. Theory, 35, 15–40, https://doi.org/10.1016/S0094-114X(99)00006-3, 2000.

Deb, K. and Jain, H.: An evolutionary many-objective optimization algorithm using reference-point-based nondominated sorting approach, part I: Solving problems with box constraints, IEEE Trans. Evol. Comput., 18, 577–601, https://doi.org/10.1109/TEVC.2013.2281535, 2013.

Deb, K., Pratap, A., Agarwal, S., and Meyarivan, T.: A fast and elitist multiobjective genetic algorithm: NSGA-II, IEEE Trans. Evol. Comput., 6, 182–197, https://doi.org/10.1109/4235.996017, 2002.

Fallahiarezoodar, N. and Zhu, Z. H.: Review of autonomous space robotic manipulators for on-orbit servicing and active debris removal, Space Sci. Technol., 5, 0291, https://doi.org/10.34133/space.0291, 2025.

Gao, Z., Zhang, D., and Ge, Y.: Design optimization of a spatial six degree-of-freedom parallel manipulator based on artificial intelligence approaches, Rob. Comput.-Integr. Manuf., 26, 180–189, https://doi.org/10.1016/j.rcim.2009.07.002, 2010.

Gosselin, C. and Angeles, J.: A global performance index for the kinematic optimization of robotic manipulators, J. Mech. Des., 113, 220–226, https://doi.org/10.1115/1.2912772, 1991.

Grewal, K. S., Dixon, R., and Pearson, J.: LQG controller design applied to a pneumatic Stewart-Gough platform, Int. J. Autom. Comput., 9, 45–53, https://doi.org/10.1007/s11633-012-0615-7, 2012.

Guo, J., Zhao, Y., Zhang, G., Liu, E., Liu, B., and Xu, Y.: Configuration synthesis and unfolding stiffness characteristics analysis of a truss antenna connecting mechanism based on URU-RR-URU hexagonal deployable unit, Mech. Mach. Theory., 177, 105047, https://doi.org/10.1016/j.mechmachtheory.2022.105047, 2022a.

Guo, J., Zhao, Y., Xu, Y., Zhang, G.: Mechanics analysis and structural design of a truss deployable antenna mechanism based on 3RR-3URU tetrahedral unit, Mech. Mach. Theory., 171, 104749, https://doi.org/10.1016/j.mechmachtheory.2022.104749, 2022b.

Holland, J.: Genetic algorithms, Sci. Am., 267, 66–73, https://doi.org/10.1038/scientificamerican0792-66, 1992.

Hornik, K., Stinchcombe, M., and White, H.: Multilayer feedforward networks are universal approximators, Neural Netw., 2, 359–366, https://doi.org/10.1016/0893-6080(89)90020-8, 1989.

Hsu, K. and Chung, C.: Singularity analysis and modular synthesis of over-constrained spatial mechanisms-A case study on Bennett and RPRP linkage, Mech. Mach. Theory, 189, 105424, https://doi.org/10.1016/j.mechmachtheory.2023.105424, 2023.

Hwang, C. L. and Yoon, K.: Multiple attribute decision making: Methods and applications a state-of-the-art survey, Springer, https://doi.org/10.1007/978-3-642-48318-9, 2012.

Ishibuchi, H., Setoguchi, Y., Masuda, H., and Nojima, Y.: Performance of decomposition-based many-objective algorithms strongly depends on Pareto front shapes, IEEE Trans. Evol. Comput., 21, 169–190, https://doi.org/10.1109/TEVC.2016.2587749, 2016.

Jin, Y.: Surrogate-assisted evolutionary computation: Recent advances and future challenges, Swarm Evol. Comput., 1, 61–70, https://doi.org/10.1016/j.swevo.2011.05.001, 2011.

Karaboga, D. and Basturk, B.: A powerful and efficient algorithm for numerical function optimization: Artificial bee colony (ABC) algorithm, J. Glob. Optim., 39, 459–471, https://doi.org/10.1007/s10898-007-9149-x, 2007.

Li, D., Wang, S., Song, X., Zheng, Z., Tao, W., and Che, J.: A bp-neural-network-based pid control algorithm of shipborne Stewart platform for wave compensation, J. Mar. Sci. Eng., 12, 2160, https://doi.org/10.3390/jmse12122160, 2024.

Liang, L., Le, Z., Zhang, S., and Li, J.: Modeling and controller design of an active motion compensated gangway based on inverse dynamics in joint space, Ocean Eng., 197, 106864, https://doi.org/10.1016/j.oceaneng.2019.106864, 2020.

Liu, G.: Optimal kinematic design of a 6-UCU kind Gough-Stewart platform with a guaranteed given accuracy, Robotics, 7, 30, https://doi.org/10.3390/robotics7020030, 2018.

Marler, R. and Arora, J.: The weighted sum method for multi-objective optimization: new insights, Struct. Multidiscip. Optim., 41, 853–862, https://doi.org/10.1007/s00158-009-0460-7, 2010.

Mu, H., Zhou, T., Li, B., and Liu, K.: Simulation and experimental study of vessel-borne active motion compensated gangway for offshore wind operation and maintenance, J. Mar. Sci. Eng., 14, 187, https://doi.org/10.3390/jmse14020187, 2026.

Niu, A., Wang, S., Sun, Y., Qiu, J., Qiu, W., and Chen, H.: Dynamic modeling and analysis of a novel offshore gangway with 3UPU/UP-RRP series-parallel hybrid structure, Ocean Eng., 266, 113122, https://doi.org/10.1016/j.oceaneng.2022.113122, 2022.

Poli, R., Kennedy, J., and Blackwell, T.: Particle swarm optimization: An overview, Swarm Intell., 1, 33–57, https://doi.org/10.1007/s11721-007-0002-0, 2007.

Pu, H., Cheng, H., Wang, G., Ma, J., Zhao, J., Bai, R., Luo, J., and Yi, J.: Dexterous workspace optimization for a six degree-of-freedom parallel manipulator based on surrogate-assisted constrained differential evolution, Appl. Soft Comput., 139, 110228, https://doi.org/10.1016/j.asoc.2023.110228, 2023.

Purshouse, R. and Fleming, P.: On the evolutionary optimization of many conflicting objectives, IEEE Trans. Evol. Comput., 11, 770–784, https://doi.org/10.1109/TEVC.2007.910138, 2007.

Qiang, H., Wang, L., Ding, J., and Zhang, L.: Multiobjective optimization of 6-DOF parallel manipulator for desired total orientation workspace, Math. Probl. Eng., 2019, 5353825, https://doi.org/10.1155/2019/5353825, 2019.

Richter, M., Schaut, S., Walser, D., Schneider, K., and Sawodny, O.: Experimental validation of an active heave compensation system: Estimation, prediction and control, Control Eng. Pract., 66, 1–12, https://doi.org/10.1016/j.conengprac.2017.06.005, 2017.

Shahbazi, M., Heidari, M., and Ahmadzadeh, M.: Optimization of dynamic parameter design of Stewart platform with Particle Swarm Optimization (PSO) algorithm, Adv. Mech. Eng., 16, 16878132241263940, https://doi.org/10.1177/16878132241263940, 2024.

Shih, H., Shyur, H., and Lee, E.: An extension of TOPSIS for group decision making, Math. Comput. Model., 45, 801–813, https://doi.org/10.1016/j.mcm.2006.03.023, 2007.

Stewart, D.: A platform with six degrees of freedom, Proc. Inst. Mech. Eng., 180, 371–386, https://doi.org/10.1243/PIME_PROC_1965_180_029_02, 1965.

Storn, R. and Price, K.: Differential evolution–a simple and efficient heuristic for global optimization over continuous spaces, J. Glob. Optim., 11, 341–359, https://doi.org/10.1023/A:1008202821328, 1997.

Tang, G., Lei, J., Li, F., Zhu, W., Xu, X., Yao, B., Claramunt, C., and Hu, X.: A modified 6-DOF hybrid serial–parallel platform for ship wave compensation, Ocean Eng., 280, 114336, https://doi.org/10.1016/j.oceaneng.2023.114336, 2023.

Tao, J., Xu, Y., Chen, Y., Cheng, P., Zhang, H., Wang, J., and Zhou, H.: Multi-objective structural parameter optimization for Stewart platform via NSGA-III and Kolmogorov-Arnold network, Machines, 1, 887, https://doi.org/10.3390/machines13100887, 2025.

Wang, D., Wang, Z., Zhao, S., Wu, N., Feng, R., and Wu, Z.: Stiffness design method of Gyroid functionally graded lattice structures based on variable porosity controlled by load path, Compos. Struct., 377, 119794, https://doi.org/10.1016/j.compstruct.2025.119794, 2026.

Wang, H., Zhang, L., Chen, G., and Huang, S.: Parameter optimization of heavy-load parallel manipulator by introducing stiffness distribution evaluation index, Mech. Mach. Theory, 108, 244–259, https://doi.org/10.1016/j.mechmachtheory.2016.10.011, 2017.

Wang, W., Ning, Y., Zhang, Y., Xu, P., and Li, B.: Linear active disturbance rejection control with linear quadratic regulator for Stewart platform in active wave compensation system, Appl. Ocean. Res., https://doi.org/10.1016/j.apor.2025.104469, 2025.

Wang, Z., Wang, C., Wu, F., Liu, Z., Liu, L., and Wang, D.: Design method of Gyroid lattice structure based on the load paths direction and capacity, Addit. Manuf., 97, 104586, https://doi.org/10.1016/j.addma.2024.104586, 2025.

Yin, L., Qiao, D., Li, B., Liang, H., Yan, J., Tang, G., and Qu, J.: Modeling and controller design of an offshore wind service operation vessel with parallel active motion compensated gangway, Ocean Eng., 266, 112999, https://doi.org/10.1016/j.oceaneng.2022.112999, 2022.

Yu, H., Lv, M., Hu, B., Zhang, Y., and Zhao, P.: A review of control technologies for soft robots: From structural design to intelligent control, Mech. Sci., 17, 313–332, https://doi.org/10.5194/ms-17-313-2026, 2026.

Zhang, L., Chen, J., Xiong, F., Ren, C., and Li, C.: Meta-learning based multi-fidelity deep neural networks metamodel method, J. Mech. Eng., 58, 190–200, https://doi.org/10.3901/JME.2022.01.190, 2022a.

Zhang, G., He, J., Guo, J., and Xia, X.: Dynamic modeling and vibration characteristics analysis of parallel antenna, Mech. Sci., 13, 1019–1029, https://doi.org/10.5194/ms-13-1019-2022, 2022b.

Zhang, G., Wang, J., Guo, J., Wang, J., Xu, Y., and Hu, F.: A novel surface division method and surface accuracy measurement for parabolic truss-type deployable antenna mechanism, Mech. Mach. Theory, 212, 106071, https://doi.org/10.1016/j.mechmachtheory.2025.106071, 2025.